Electromechanically Induced GHz Rate Optical Frequency Modulation in Silicon
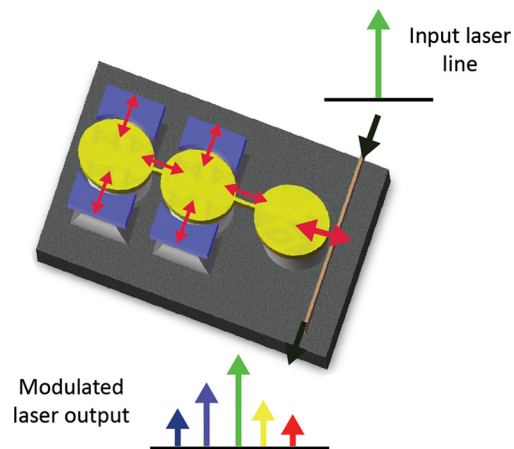
Volume 4, Number 5, October 2012

S. Tallur, Student Member, IEEE
S. A. Bhave, Member, IEEE

Electromechanically Induced GHz Rate Optical Frequency Modulation in Silicon

S. Tallur, *Student Member, IEEE*, and S. A. Bhave, *Member, IEEE*

Department of Electrical and Computer Engineering, OxideMEMS Lab,
Cornell University, Ithaca, NY 14850 USA

Abstract: We present a monolithic silicon acousto-optic frequency modulator (AOFM) operating at 1.09 GHz. Direct spectroscopy of the modulated laser power shows asymmetric sidebands, which indicate coincident amplitude modulation and frequency modulation (FM). Employing mechanical levers to enhance the displacement of the optical resonator resulted in greater than 67X improvement in the optomechanical FM factor over earlier reported numbers for silicon nanobeams.

Index Terms: Silicon optomechanics, optical frequency modulation (FM).

1. Introduction

Optical frequency modulation (FM) has been achieved in microstructures using surface acoustic waves to strain self-assembled InAs/GaAs quantum dots [1], [2]. Photon generation at > GHz frequency spacing from a single pump laser has been realized in silicon nitride and silicon dioxide via nonlinear optical processes such as the optical Kerr effect [3] and stimulated Brillouin scattering [4], [5]. It is difficult to exploit such nonlinear optical phenomena in silicon, primarily owing to two-photon absorption that limits optical power handling. Wavelength conversion in silicon has been demonstrated using fundamentally all-optical schemes [6], [7] and via free-carrier plasma dispersion effect [8], making their integration on microelectronic chips challenging.

Electrostatic capacitive actuation and detection is the main scheme of transduction used in radio frequency (RF) microelectromechanical systems (MEMS) resonators [9]–[11]. The use of electrostatics enables direct integration with electronics used for processing RF signals. Electrostatic capacitive actuation of optomechanical resonators has been demonstrated earlier using a standalone optomechanical system with a gradient electrical force on a dielectric provided by an off-chip electrode [12] and using integrated electrodes [13]–[15]. Employing this scheme at GHz rates will provide valuable narrow-band acousto-optic modulators for direct conversion of electrical signals to optical intensity modulation that are valuable toward realizing a chip-scale optoelectronic oscillator (OEO) [16]. In addition to intensity modulation, it is desirable to achieve FM, which adds variable group delay into the optical field, thus potentially boosting phase noise performance of the OEO [17]. In this paper, we present a monolithic integrated silicon acousto-optic frequency modulator designed in a silicon-on-insulator (SOI) platform. The modulator bandwidth is governed by the quality factor of the mechanical resonance. This design can open up avenues toward realizing a truly chip-scale OEO and enable on-chip dense wavelength division multiplexing (DWDM) using a single input laser. The next section
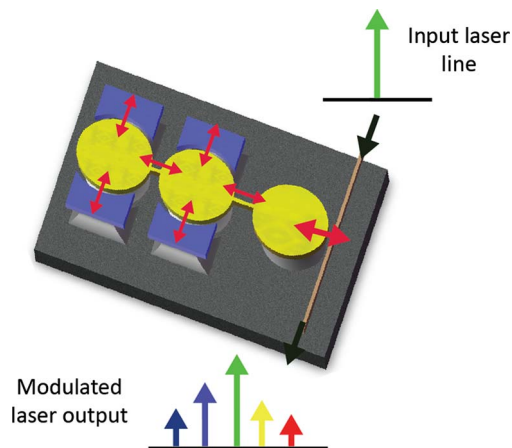
Fig. 1. Illustration of the acousto-optic frequency modulator showing generation of laser sidebands by acoustically exciting motion of the coupled optomechanical resonator via electrostatic capacitive transduction. The motion of the optomechanical cavity results in phase modulation of the light field resulting in generation of multiple sidebands around the laser line.

presents the theoretical basis for the operation of this device. In later sections, we describe the device design and experimental results.

2. Theoretical Treatment of Optomechanical Modulation

Silicon optomechanical resonators operated in the resolved sideband regime stand out as strong candidates for optical FM owing to their strongly coupled mechanical and optical degrees of freedom [18]. This coupling mechanism is nonlinear, and the nonadiabatic response of the intracavity optical field to changes in the cavity size can lead to modification of its mechanical dynamics. On the other hand, if the mechanical resonant mode of the cavity is actuated, the cavity executes oscillatory motion at this frequency, which results in the Doppler shift of the circulating intracavity optical field, thus modulating its phase. In the frequency domain, this FM manifests itself as sidebands centered about the input laser frequency line, at a frequency separation that is equal to the frequency of the actuated mechanical resonance. The cavity density of states shapes the resultant sidebands leading to enhancement of only those sidebands that are coupled to the optical cavity, thus causing an asymmetry in the intensity of the lower and higher frequency sidebands. This asymmetry leads to an effective amplitude modulation (AM) of the laser light, in addition to FM. Fig. 1 shows an illustration of such a scheme using electrostatic actuation. This section deals with the theoretical treatment of this phenomenon.

2.1. Electrostatically Induced Optomechanical Modulation

The microdisk resonators on the left of Fig. 1 are flanked by electrodes to provide electrostatic actuation to drive the mechanical modes. Applying a combination of dc bias voltage V_{DC} and ac signal v_{AC} results in the generation of a force acting on the disk in the radial direction, at the frequency of the applied ac voltage ω_{AC}, i.e.,

$$F(\omega_{\text{AC}}) = \frac{dC_g}{dg} V_{\text{DC}} v_{\text{AC}} \tag{1}$$

where dC_g/dg is the change in the actuation capacitance C_g for a small change in the electrode-resonator capacitor gap g. If the frequency of the applied ac voltage corresponds to the frequency of a

mechanical mode of the resonator, the force results in a radial displacement at the mechanical resonantor frequency, as shown in (2), i.e.,

$$\Delta r(\omega_{\text{AC}}) = \frac{Q_{\text{mech}} F(\omega_{\text{AC}})}{K_r}. \tag{2}$$

Here, Q_{mech} denotes the quality factor of the mechanical resonance, and K_r represents the mechanical stiffness (effective spring constant) of the radial vibrational mechanical mode. These vibrations are mechanically coupled into the optomechanical cavity resonator on the right, which is probed by coupling laser light to an optical resonant mode of the cavity. The sensitivity of the optomechanical resonator to radial displacement is obtained from the optical resonance condition, i.e.,

$$m\lambda_{\text{opt}} = 2\pi R n_{\text{eff}} \tag{3}$$

where m is an integer, λ_{opt} is the free space wavelength of the optical resonant mode, R is the radius of the optomechanical resonator, and n_{eff} is the effective refractive index for the mode. Displacement $\Delta r(\omega_{\text{AC}})$ results in a shift in optical resonance wavelength of $\Delta\lambda_{\text{opt}} = (\Delta r(\omega_{\text{AC}})/R)\lambda_{\text{opt}}$. This can be also quantified by defining an equivalent optomechanical coupling coefficient, i.e.,

$$g_{\text{om}} = \frac{d\omega_{\text{opt}}}{dR} = -\frac{d\lambda_{\text{opt}}}{dR} \tag{4}$$

where ω_{opt} is the frequency of the input pump laser. The mechanical vibration of the resonator is detected as modulation of the input laser light, as detailed in the following subsection.

2.2. Transmission of an Optomechanical Cavity

Assume that the cavity is oscillating at the mechanical resonant frequency Ω_0, such that its radius is sinusoidally displaced as described in (5), i.e.,

$$u(t) = U_0 \sin(\Omega_0 t). \tag{5}$$

The amplitude of the light field circulating inside the optomechanical cavity $a_p(t)$ can be derived as in [19] by introducing a modulation index $\beta = (U_0/R)(\omega_{\text{opt}}/\Omega_0)$, i.e.,

$$a_p(t) = \frac{s}{\sqrt{\tau_{\text{ex}}}} \sum_{n=-\infty}^{+\infty} \frac{(-i)^n J_n(\beta)}{\frac{\kappa}{2} + i(\Delta + n\Omega_0)} \exp\left[i(\omega_{\text{opt}} + n\Omega_0)t + i\beta\cos(\Omega_0 t)\right] \tag{6}$$

where s denotes the input pump laser field amplitude, τ_{ex} is the photon lifetime due to coupling between the cavity and the waveguide, κ is the full width at half maximum (FWHM) linewidth of the optical cavity resonance, and Δ denotes the detuning of the laser from the optical cavity resonance, specified in angular frequency. Thus, the modulation index determines the relative weights of the sidebands, whose width is governed by the optical cavity linewidth.

Of particular interest are the cases where $\kappa/2 \gg (\Delta + \Omega_0)$ and $\kappa/2 \ll (\Delta + \Omega_0)$. The former case corresponds to unresolved motional sidebands. Noting that $J_{-n}(\beta) = (-1)^n J_n(\beta)$, it is easy to see that the lower and higher frequency primary sidebands are in phase with each other, resulting in predominant AM. In the latter case of resolved motional sidebands, the phase relationship is reversed, leading to predominant FM. For other detuning values, the sidebands are highly asymmetric in the resolved sideband regime. When the detuning is zero, the motion of the optomechanical cavity leads to pure phase modulation of the laser light. For nonzero detuning, the cavity density of states leads to an asymmetry in the relative sideband intensities. This asymmetry is associated with coincidental AM and FM of the laser light [20], as explained in the following subsection.

2.3. Coincidental AM and FM

Consider a sine wave carrier expressed by the following general equation:

$$s(t) = A \cos(\omega_c t). \tag{7}$$

A is the amplitude and ω_c is the frequency of the carrier signal. When the signal is amplitude-modulated with a modulation index m_{AM} at frequency ω_m, the expression for the modulated signal can be written as follows:

$$
\begin{aligned}
s_{AM}(t) &= A[1 + m_{AM}\cos(\omega_m t)]\cos(\omega_c t) \\
&= A\cos(\omega_c t) + \frac{m_{AM}A}{2}\cos[(\omega_c + \omega_m)t] + \frac{m_{AM}A}{2}\cos[(\omega_c - \omega_m)t].
\end{aligned} \tag{8}
$$

Thus, AM generates symmetric sidebands around the carrier at frequencies $\omega_c + \omega_m$ and $\omega_c - \omega_m$. For 100% modulation, i.e., $m_{AM} = 1$, the amplitude of each band is half that of the carrier, which corresponds to 6-dB lower power than the carrier. In AM, all the power injected into the signal via the modulating signal is added at the sidebands, without affecting power at the carrier frequency.

Consider the FM of the carrier at frequency ω_m with a modulation index m_{FM}. The modulated signal now has multiple frequency components, i.e.,

$$
\begin{aligned}
s_{FM}(t) &= A[\cos(\omega_c t + m_{FM}\sin(\omega_m t))] \\
&= A[\cos(\omega_c t)\cos(m_{FM}\sin(\omega_m t)) - \sin(\omega_c t)\sin(m_{FM}\sin(\omega_m t))].
\end{aligned} \tag{9}
$$

Using the Fourier series expansions $\cos(m_{FM}\sin(\omega_m t)) = \sum_{n=0}^{\infty} 2nJ_{2n}(m_{FM})\cos(2n\omega_m t)$ and $\sin(m_{FM}\sin(\omega_m t)) = \sum_{n=0}^{\infty} 2J_{2n+1}(m_{FM})\sin([2n+1]\omega_m t)$, we can express the signal in terms of all its frequency components, i.e.,

$$s_{FM}(t) = A\left[J_0(m_{FM})\cos(\omega_c t) + \sum_{n=0}^{\infty}(-1)^n J_n(m_{FM})\Big[\cos((\omega_c - n\omega_m)t) + (-1)^n\cos((\omega_c + n\omega_m)t)\Big] \right]. \tag{10}$$

The expression highlights the phase relation between all the frequency components. Each sideband is characterized by its order n. The vector sums of the odd-order sideband pairs are always in quadrature with the carrier component of the signal, and the vector sums of the even-order sideband pairs are always collinear with the carrier component. The phase shift for the odd-order sidebands arises from the reversal of the phase for the lower frequency sidebands with respect to the higher frequency sidebands. The power in the lower and higher frequency sidebands is the same for sidebands of all order. Unlike AM, FM affects the power at the carrier frequency. FM does not involve injecting power into the signal; the modulating signal results in redistribution of the power at the carrier frequency into all the sidebands. From (8) and (10), it is clear that, if a signal has coincidental AM and FM, the higher and lower frequency sidebands of the first order are asymmetric, i.e., the power in the higher frequency sideband is different from the power in the lower frequency sideband. The mismatch in power depends on the phase relationship between the AM and FM processes. It is also interesting to note the effect of introducing asymmetry in the intensities of lower and higher frequency sidebands in (10). The amplitude of the resulting signal is no longer constant and has AM in addition to FM.

3. Device Design

3.1. Mechanical Displacement Amplification

A silicon acousto-optic modulator (AOM) with a mechanical resonance frequency of 1.1 GHz has been presented [21]. This device has an optical cavity of 3 dB and a linewidth of $\approx$5.88 GHz and
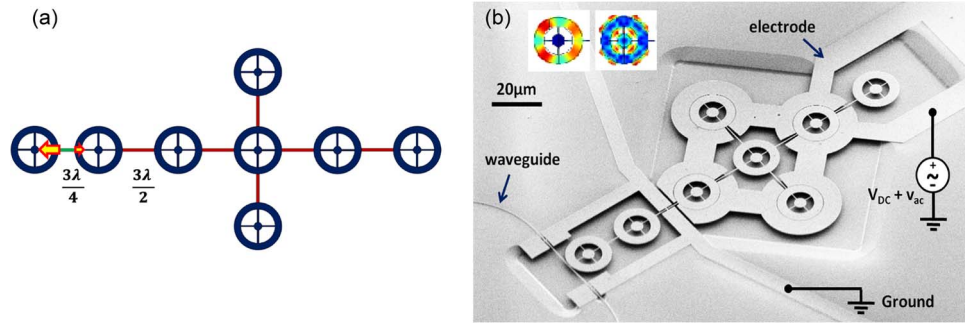
Fig. 2. (a) Illustration of the micromechanical displacement amplifier. The three-quarter-wavelength coupling beam connecting the output optomechanical resonator on the left to the array composite of drive micromechanical resonators on the right ensures mechanical displacement amplification. (b) SEM of the fabricated acousto-optic frequency modulator (AOFM). Insets: Finite element simulation (FEM) of the mechanical mode shape of the ring at 176 MHz (left - fundamental radial expansion mode) and 1.09 GHz (right - compound radial expansion mode).

results in predominant AM of the laser light. For efficient FM, we want the device to operate in the resolved sideband regime. If the laser frequency is detuned to the FWHM point of the optical resonance ω_{opt}, the modulation depth depends linearly on the motion-induced frequency shift. The optomechanical coupling coefficient for a microring resonator is given by $g_{om} = (d\omega_{opt}/dR) = -(\omega_{opt}/R)$, where R is the radius of the microring. Thus, larger mechanical displacement translates to greater shift in the resonance frequency, thereby enhancing the modulation depth. Hence, it is desirable to get large mechanical displacements, in addition to operating in the resolved sideband regime, to achieve efficient FM.

The modulator presented in [21] is extended to an array of mechanically coupled ring resonators for large electrostatic driving force. We also use a mechanical lever system [22] to realize displacement amplification. An array composite of rings on the input electrostatic side feeds via an acoustic quarter-wavelength coupling beam into a single output optomechanical ring resonator, as illustrated in Fig. 2(a).

Consider an array of N ring resonators strongly coupled to each other using half-wavelength coupling beams. The effective stiffness of the composite resonator defined by the array is $K_{eff} = NK_r$, where K_r is the stiffness of each individual ring. Coupling this array to another ring resonator using a quarter-wavelength coupling beam results in a mismatch of the stiffnesses on either side of this coupling beam. A quarter-wavelength coupling beam, by definition, forces the velocity at both ends of the beam to be the same. Thus, the kinetic energy of the moving ends of the coupling beam and, hence, the stored potential energy in the resonators on either end of the beam are the same. Thus, if x_o is the radial displacement of the output optomechanical ring resonator and x_{array} is the radial displacement of each ring resonator in the array, the energy constraint ensures:

$$\frac{1}{2}K_r x_o^2 = \frac{1}{2}K_{eff}x_{array}^2 \tag{11}$$

$$\Rightarrow \frac{x_o}{x_{array}} = \sqrt{N}. \tag{12}$$

Thus, the difference in stiffnesses of the input array and output ring results in an enhancement of the displacement at the output.[1]

---

[1]The coupling beam lengths are designed to correspond to three halves of the acoustic wavelength for strong coupling, and three quarters of the acoustic wavelength at 1.09 GHz for the displacement amplification beam. These dimensions are chosen for making the layout of the rings feasible. Choosing such a geometry does not affect the displacement amplification scheme.
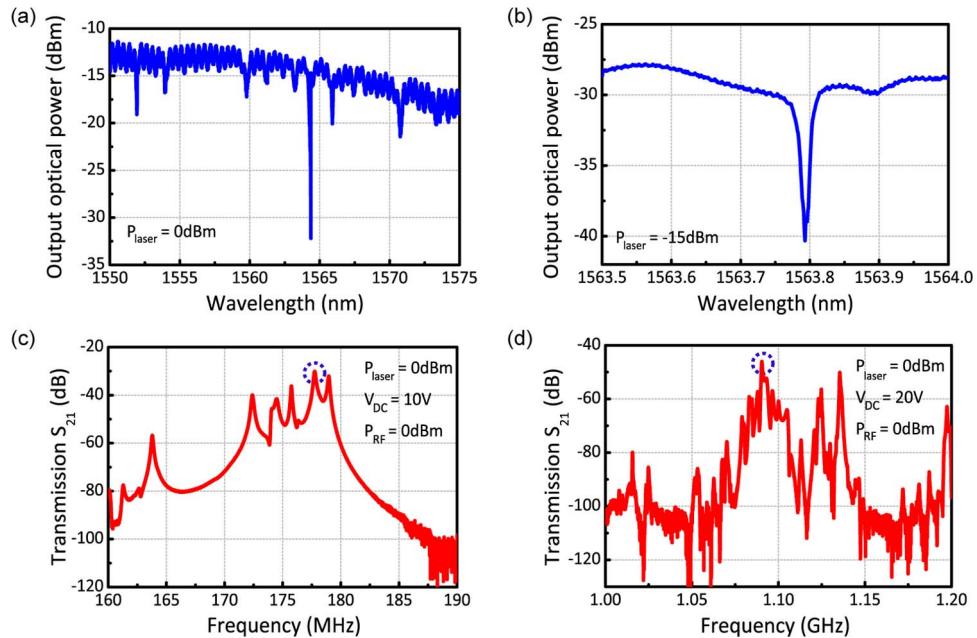
Fig. 3. (a) Various resonances for the optomechanical cavity are observed in the optical transmission spectrum as the laser wavelength is swept from 1,550 nm to 1,575 nm. (b) Critically coupled optical resonance at 1,563.8 nm with loaded optical $Q \approx 150{,}000$, probed with an input laser power of -15 dBm. (c) Transmission of the modulator measured from 160 MHz to 190 MHz. The fundamental radial expansion mode of the ring has an insertion loss of 30 dB, seen here in the transmission spectrum (circled). (d) Transmission of the modulator measured from 1 GHz to 1.2 GHz. The compound radial expansion mode of the ring has an insertion loss of 46 dB (circled). Multiple peaks are seen as a result of imperfections in the beam lengths on account of fabrication variations. All experiments were performed under atmospheric pressure at room temperature.

3.2. Fabrication Process

This section describes how the modulator is fabricated. The procedure involves a three-mask process flow on a custom SOI wafer (undoped 250-nm device layer for low optical loss and 3-μm-thick buried oxide for isolation of the device from the silicon substrate). The top silicon is thermally oxidized to obtain a thin oxide hard mask layer with a thickness of 60 nm atop a 220-nm-thick silicon device layer. The ma-N 2403 electron beam resist is spun on top of the oxide and patterned using electron beam lithography. The patterns are transferred into the silicon dioxide using a CHF_3/O_2-based reactive ion etcher and then into the silicon device layer using a chlorine based reactive ion etch. A layer of SPR-220 3.0 photoresist is spun, and a second mask is used to pattern windows above the mechanical resonator, the electrical routing beams and the bond pads. This is followed by a boron ion implantation and nitrogen anneal to reduce the resistivity of these structures. A third mask is then used to pattern release windows near the modulator using SPR-220 3.0 photoresist, followed by a timed release etch in buffered oxide etchant to undercut the devices. The samples are then dried using a critical point dryer to prevent stiction. Fig. 2(b) shows a scanning electron micrograph (SEM) of the fabricated device.

4. Experimental Setup and Results

4.1. Characterization of the Modulator

To probe the optical response of the modulator, light from a Santec TSL-510 tunable laser polarized parallel to the substrate is coupled into the waveguide using grating couplers. The optical output power is measured to obtain the optical transmission spectrum of the device. As shown in Fig. 3(a) we observe multiple dips corresponding to various modes of the optical cavity. We choose
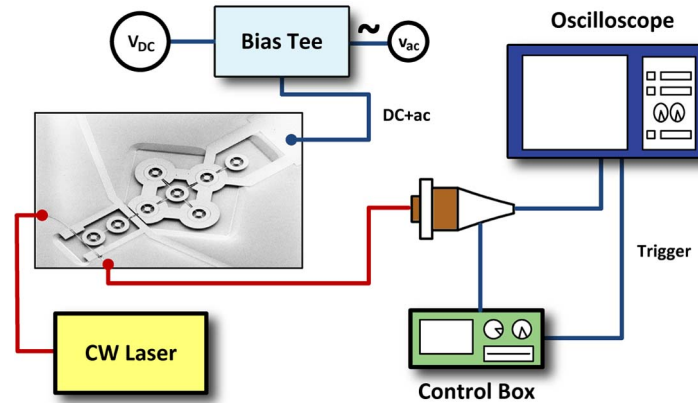
Fig. 4. Experimental setup for characterization of the optical sidebands of the modulator using a scanning FP interferometer. The frequency of the applied ac voltage corresponds to the resonance frequency of the mechanical mode of interest [circled in Fig. 3(c) and (d)].

the critically coupled optical resonant mode at a wavelength around 1,564 nm with a total optical quality factor of ≈150,000 and an extinction of 10 dB, as seen in Fig. 3(b). This corresponds to a FWHM cavity linewidth of 1.27 GHz. To identify the mechanical modes of the resonator, we characterize the RF transmission of the response of the modulator using a network analyzer. A bias tee is used to apply a combination of dc bias voltage along with ac power from port 1 of an Agilent N5230A network analyzer at the probe pads of the electrode with a Cascade GSG RF probe. The tunable laser is blue detuned to the half maximum point of the optical cavity. Mechanical motion of the device induced by the applied input voltage translates into intensity modulation of the laser light, which is picked off and converted into electrical RF signal by a Newport 1544-A near-IR photoreceiver connected at the output of the modulator. The output of the photoreceiver is connected to port 2 of the network analyzer. The RF is swept and the transmission spectrum for the modulator is recorded, as shown in Fig. 3(c) and (d). The mechanical quality factors measured for these resonant modes are 800 and 1,800, respectively. The coupling beams are designed for optimal displacement amplification of the mechanical mode with a frequency of 1.09 GHz.

4.2. Characterization of the Optical Sidebands

For observing the motion-generated optical sidebands for the modulator, we use a Thorlabs SA210-12B scanning Fabry–Perot (FP) interferometer. The confocal design of this FP interferometer cavity is relatively insensitive to the alignment of the input beam. The tunable laser is blue detuned to the optical cavity and a bias tee is used to apply a combination of dc bias voltage and ac voltage at the resonance frequency of the mechanical mode [circled in Fig. 3(c) and (d)] using an Agilent E8257D PSG Analog Signal Generator. Using an SA201 control box for the FP interferometer, the wavelength of the FP cavity is scanned across its entire range by sweeping the voltage on the piezocontroller in the control box. The transmitted light intensity is measured using an internal photodiode, amplified by a transimpedance amplifier inside the control box, and displayed on an oscilloscope. As the FP cavity scans across wavelengths, its output on an oscilloscope shows a peak whenever it passes across a sideband. The controller also provides a trigger signal to the oscilloscope, which allows the oscilloscope to easily trigger at the beginning or the middle of the scan. The free spectral range (FSR) of the FP interferometer that we use is 1.5 GHz, and this information is used to scale the x-axis of the oscilloscope output from units of time to frequency offset from pump laser. The root mean square (RMS) noise voltage of the photo-amplifier in the control box is 1.5 mV for a gain setting of 1 MV/A. The measured FSR for the cavity is 7.2 ms, and the FWHM linewidth is 35 μs, which correspond to 1.5 GHz and 7.2 MHz, respectively, and cavity finesse of 205. An illustration of the experimental setup is shown in Fig. 4.
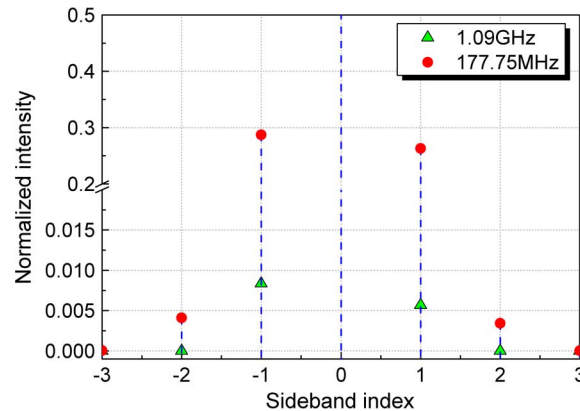
Fig. 5. Calculated spectrum for the modulator response at 177.75 MHz and 1.09 GHz for relative detuning of 0.5. A combination of 10 V dc and 5 dBm ac power was considered at the input electrode for operation at 177.75 MHz, and a combination of 20-V dc and 8-dBm ac power was accounted for at 1.09 GHz. The primary sideband intensities are highly asymmetric for operation at 1.09 GHz. The Y-axis has a break between 0.02 and 0.2 to clearly show the sideband intensities at both frequencies.
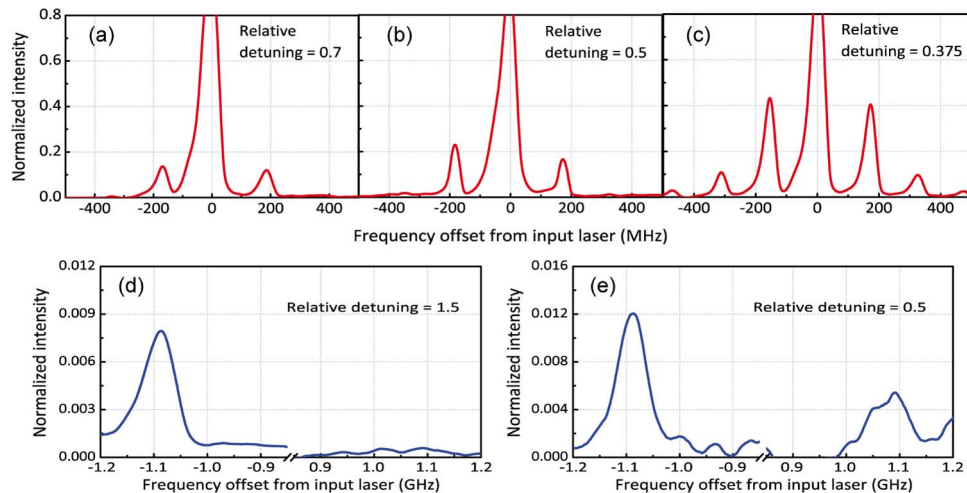

Fig. 6. Measured optical spectrum at output of the modulator using a scanning FP interferometer. (a)–(c) When operated at 177.75 MHz for relative detuning values 0.7, 0.5 and 0.375, we observe almost symmetric lower and higher frequency sidebands in the optical spectrum on account of AM of the laser light. A combination of 10-V dc and 5-dBm ac power was applied at the input electrode. The distorted shape of the laser line is an artifact of the scan. (d) and (e) The sidebands are highly asymmetric in the case of operation at 1.09 GHz, which corresponds to resolved motional sidebands. Relative detuning of 1.5 corresponds to detuning on the order of the mechanical resonant frequency, resulting in maximum asymmetry. A combination of 20-V dc and 8-dBm ac power was applied at the input electrode. The FSR of the FP interferometer used here is 1.5 GHz, which leads to aliasing from adjacent sweeps and hence we only show the region of interest around ±1.09 GHz.

    Fig. 5 shows the calculated frequency spectrum showing the intensities of the sidebands for the modulator normalized to the input pump laser intensity for operation and 177.75 and 1.09 GHz using (6). The relative detuning, defined as $2\Delta/\kappa$, is set to 0.5. The displacement amplitude was calculated by following the derivation in [23]. A displacement amplification factor of $\sqrt{7}$ was accounted for displacement at 1.09 GHz.

    Fig. 6 shows measured sideband intensities for the two mechanical modes measured at different relative detuning values. Panels (a)–(c) show recorded optical sidebands at 177.75 MHz. As expected, the asymmetry in the sidebands is very small for this mechanical resonant mode of the

optomechanical cavity, on the account of unresolved motional sidebands. A combination of 10-V dc and 5-dBm ac power was applied at the input electrode of the modulator. Maximum asymmetry is observed for a relative detuning value of 0.5, which corresponds to the half maximum point of the optical cavity resonance. This is in sharp contrast to the highly asymmetric intensities observed in case of the mechanical resonant mode at 1.09 GHz, as shown in panels (d) and (e). A combination of 20-V dc and 8-dBm ac power was applied at the electrodes in this case. The asymmetry confirms the coexistence of AM and FM in the light field at the output of the modulator. The apparent mismatch in frequency of the positive and negative frequency sidebands is an artifact of the scan rate of the FP interferometer. It is possible to realize perfect FM with no AM by setting the detuning of the laser with respect to the cavity to zero, but this requires additional feedback loops, such as the Hansch–Couillaud technique [19]. The FM factor (modulation index) for an optomechanical cavity was defined in (6) as $\beta = (g_{\mathrm{om}}/\Omega_0)$. The measured FM factor for our modulator operated at 1.09 GHz is 0.067, which corresponds to a greater than 67X improvement over earlier reported numbers for silicon nanobeams [24]. This large modulation factor is significant for efficiently generating multiple laser lines in silicon.

5. Conclusion

In conclusion, we demonstrate FM at 1.09 GHz of a continuous wave laser at 1,564 nm using a coupled optomechanical silicon resonator. The monolithic integrated design augurs well for CMOS compatible processing of such modulators. This work constitutes the first demonstration of electroacoustically generating photons of different colors from a single pump laser in silicon. The acoustic-actuation mechanism in the modulator presented here is narrowband and governed by the mechanical quality factor. Our modulator design generates multiple laser lines, with a frequency separation governed precisely by the mechanical resonant frequency. Scaling the modulator to an internal dielectric transduced resonator design [25] will enable generation of laser lines at higher frequencies in the range of 25–50 GHz for applications in DWDM networks.

Acknowledgment

References

[1] D. A. Fuhrmann, S. M. Thon, H. Kim, D. Bouwmeester, P. M. Petroff, A. Wixforth, and H. J. Krenner, "Dynamic modulation of photonic crystal nanocavities using gigahertz acoustic phonons," *Nat. Photon.*, vol. 5, no. 10, pp. 605–609, Oct. 2011.

[2] M. Metcalfe, S. M. Carr, A. Muller, G. S. Solomon, and J. Lawall, "Resolved sideband emission of InAs/GaAs quantum dots strained by surface acoustic waves," *Phys. Rev. Lett.*, vol. 105, no. 3, p. 037401, Jul. 2010.

[3] T. J. Kippenberg, R. Holzwarth, and S. A. Diddams, "Microresonator-based optical frequency combs," *Science*, vol. 332, no. 6029, pp. 555–559, Apr. 2011.

[4] G. Bahl, J. Zehnpfennig, M. Tomes, and T. Carmon, "Stimulated optomechanical excitation of surface acoustic waves in a microdevice," *Nat. Commun.*, vol. 2, p. 403, Jul. 2011.

[5] H. Lee, T. Chen, J. Li, K. Y. Yang, S. Jeon, O. Painter, and K. J. Vahala, "Chemically etched ultrahigh-Q wedge-resonator on a silicon chip," *Nat. Photon.*, vol. 6, no. 6, pp. 369–373, May 2012.

[6] B. Jalali, V. Raghunathan, and O. Boyraz, "Raman-based silicon photonics," *IEEE J. Sel. Topics Quantum Electron.*, vol. 12, no. 3, pp. 412–421, May/Jun. 2006.

[7] Q. Xu, V. R. Almeida, and M. Lipson, "Micrometer-scale all-optical wavelength converter on silicon," *Opt. Lett.*, vol. 30, no. 20, pp. 2733–2735, Oct. 2005.

[8] S. F. Preble, Q. Xu, and M. Lipson, "Changing the colour of light in a silicon resonator," *Nat. Photon.*, vol. 1, no. 5, pp. 293–296, May 2007.

[9] J. Wang, Z. Ren, and C. T.-C. Nguyen, "1.156-GHz self-aligned vibrating micromechanical disk resonator," *IEEE Trans. Ultrason., Ferroelectr., Freq. Control*, vol. 51, no. 12, pp. 1607–1628, Dec. 2004.

[10] J. R. Clark, W.-T. Hsu, M. A. Abdelmoneum, and C. T.-C. Nguyen, "High-Q UHF micromechanical radial-contour mode disk resonators," *J. Microelectromech. Syst.*, vol. 14, no. 6, pp. 1298–1310, Dec. 2005.

[11] S. Pourkamali, Z. Hao, and F. Ayazi, "VHF single-crystal silicon capacitive elliptic bulk-mode disk resonators—Part II: Implementation and characterization," *J. Microelectromech. Syst.*, vol. 13, no. 6, pp. 1054–1062, Dec. 2004.

[12] K. H. Lee, T. G. McRae, G. I. Harris, J. Knittel, and W. P. Bowen, "Cooling and control of a cavity optoelectromechanical system," *Phys. Rev. Lett.*, vol. 104, no. 12, p. 123 604, Mar. 2010.

[13] S. Sridaran and S. A. Bhave, "Electrostatic actuation of silicon optomechanical resonators," *Opt. Exp.*, vol. 19, no. 10, pp. 9020–9026, 2011.

[14] J. Yao, D. Leuenberger, M.-C. M. Lee, and M. C. Wu, "Silicon microtoroidal resonators with integrated MEMS tunable coupler," *IEEE J. Sel. Topics Quantum Electron.*, vol. 13, no. 2, pp. 202–208, Mar./Apr. 2007.

[15] R. Perahia, J. D. Cohen, S. Meenehan, T. P. M. Alegre, and O. Painter, "Electrostatically tunable optomechanical "zipper" cavity laser," *Appl. Phys. Lett.*, vol. 97, no. 19, p. 191 112, Nov. 2010.

[16] X. S. Yao and L. Maleki, "Optoelectronic oscillator for photonic systems," *IEEE J. Quantum Electron.*, vol. 32, no. 7, pp. 1141–1149, Jul. 1996.

[17] J. Yu, X. S. Yao, and L. Maleki, "Compact optoelectronic oscillator with ultra-low phase noise performance," *Electron. Lett.*, vol. 35, no. 18, pp. 1554–1555, Sep. 1999.

[18] T. J. Kippenberg and K. J. Vahala, "Cavity opto-mechanics," *Opt. Exp.*, vol. 15, no. 25, pp. 17 172–17 205, Dec. 2007.

[19] A. Schliesser, R. Rivière, G. Anetsberger, O. Arcizet, and T. J. Kippenberg, "Resolved-sideband cooling of a micromechanical oscillator," *Nat. Phys.*, vol. 4, no. 5, pp. 415–419, May 2008.

[20] H. Roder, "Amplitude, phase, and frequency modulation," *Proc. Inst. Radio Eng.*, vol. 19, no. 12, pp. 2145–2176, Dec. 1931.

[21] S. Sridaran and S. A. Bhave, "1.12 GHz opto-acoustic oscillator," in *Proc. 25th IEEE Int. Conf. MEMS*, 2012, pp. 664–667.

[22] W.-C. Li, I. Gurin, S.-S. Li, Y.-W. Lin, Z. Ren, B. Kim, and C. T.-C. Nguyen, "Digitally-specified micromechanical displacement amplifiers," in *Proc. Int. TRANSDUCERS*, 2009, pp. 781–784.

[23] S. Tallur, T. J. Cheng, S. Sridaran, and S. A. Bhave, "Motional impedance analysis: Bridging the "Gap" in dielectric transduction," in *Proc. Joint Conf. IEEE Int. FCS*, 2011, pp. 1–4.

[24] J. Chan, T. P. M. Alegre, A. H. Safavi-Naeini, J. T. Hill, A. Krause, S. Gröblacher, M. Apselmeyer, and O. Painter, "Laser cooling of a nanomechanical oscillator into its quantum ground state," *Nature*, vol. 478, no. 3767, pp. 89–92, Oct. 2011.

[25] D. Weinstein and S. A. Bhave, "The resonant body transistor," *Nano Lett.*, vol. 10, no. 4, pp. 1234–1237, 2010.